JOURNAL OF MATERIALS SCIENCE **37** (2002) 1575–1583

Finite element analysis of a polymer composite subjected to a sliding steel asperity

Part I *Normal fibre orientation*

TIBOR GODA, KÁROLY VÁRADI
Institute of Machine Design, Budapest University of Technology and Economics, H-1111 Budapest, Műegyetem rkp. 3, Hungary
E-mail: varadik@eik.bme.hu

KLAUS FRIEDRICH, HERMANN GIERTZSCH
Institute for Composite Materials Ltd. (IVW), University of Kaiserslautern, D-67663 Kaiserslautern, Erwin-Schrödinger str. Geb. 58, Germany
E-mail: friedrich@ivw.uni-kl.de

FE micro-models have been developed in order to determine contact, stress and strain conditions produced by a steel asperity sliding on the surface of a normally oriented fibre-reinforced polymer composite. A displacement coupling technique was introduced to model a "micro-environment" as part of a "macro-environment" and to get more realistic simulation results about the failure conditions in the composite structure, in comparison to the so far widely applied anisotropic analytical or numerical macro-models. On the basis of the results, conclusions may be drawn for the possible wear mechanisms of the fibre-reinforced polymer composite. Stress results in the vicinity of the fibers in the contact area show high shear loading of the matrix leading to the formation of stretched-out matrix wear debris. In addition, high repeated compression-tension stresses at the fibre/matrix interface near the surface can lead to fibre debonding phenomena. Considering the fibre ends in the contact region, high compression stresses at their rear edges can produce fibre cracking features. To study the wear mechanisms experimentally, a "single asperity" scratch test was also performed showing shear failure events of the polymer matrix, fibre/matrix debonding and fibre cracking effects, as expected from the modelling studies.

1. Introduction

In the course of the past few decades, polymer based composites with short or continuous fibre reinforcement have been increasingly used in various fields, including different tribological applications. The friction and wear behavior of these materials has been intensively studied recently, in order to improve their tribological performance. In particular, intensive research was performed in order to get a better understanding of the wear processes in the case of composites against steel counterparts. Since the contact, stress and deformation characteristics during sliding contact have a considerable impact on the wear behavior of structural elements it is important to evaluate these conditions in a more accurate way.

Fibre-reinforced composites are generally characterized by the fact that they are inhomogeneous and have direction-dependent mechanical properties. Analytical approaches (e.g. [1–4]) usually apply the widely used approximation to substitute the originally inhomogeneous material structure by homogeneous, anisotropic material properties obtained by the so-called rule of mixtures formulae [1]. A disadvantage of this macroscopic approach is that it is not suitable for modelling the actual interaction of the fibers and matrix of the composite with the asperities of the steel counterpart.

To study the contact and stress states of fibre-reinforced composites, Keer and Mowry [2] presented an analytical solution by using an anisotropic half-space model. Ovaert and Wu [3, 4] also used relationships based on the macroscopic approach to determine stresses produced in the composite material when a steel ball, modelling an asperity, was slid along a homogeneous, transversely isotropic half-space, modelling a normally oriented fibre-reinforced composite. According to their conclusions, fibre debonding at the rear part of the contact area may be caused in the composite by tensile stresses parallel to the sliding direction. According to their failure criterion, fibre debonding is produced when the tensile stress peak, multiplied by a stress concentration coefficient, exceeds the tensile strength of the fibre/matrix interface. The authors used this stress concentration coefficient in order "to step into the microscopic world" containing actual fibre/matrix contacts.

In [5], a FE micro-model was developed in order to determine contact and stress states produced by a steel ball pressed into a fibre-reinforced composite. Location and distribution of sub-surface stresses and strains were studied for normal (N) as well as parallel (P) fibre orientation. It was established that in the case of normal (N) fibre orientation there is a high shear stress region below the surface, from where the fibre/matrix interfacial failure initiates before propagating to the surface.

The present study aims at the development of FE micro-models for the description of different failure mechanisms in continuous fibre-reinforced polymer composites, when being slid under N fibre orientation against a steel counterpart (of which the roughness is modeled by a sliding hemispheric asperities). In particular, it is expected that this approach will give answers about the actual fibre stresses, matrix strains, events of fibre/matrix debonding and other characteristic wear mechanisms in normally oriented fibre-reinforced polymer composites, as shown in Fig. 1. TFL means transfer film layer that is a layer of compacted wear debris.

It should be mentioned, however, that the FE contact/stress analysis of fibre/matrix micro-structures is rather limited. Even if a very small-sized (e.g. 100 μm $\times$ 50 μm $\times$ 50 μm) FE micro-model is used, the degree of freedom (DOF) may reach 100 000. To combine such a micro-model structure with the model of the actual structural component, this "micro-environment" can be "interconnected" by an approximate displacement coupling technique [5]. In this way, a system of a micro-model "built into" a macro environment can be created, in order to achieve more accurate results.

The composite material studied here is a CF (carbon fibre) reinforced PEEK (polyether-etherketone) with a fibre volume fraction of 0.61. Its mechanical properties along with those of the steel asperity are listed in Table I. The first principal material direction, indicated by 1 in Table I, is parallel to the z-axis (Fig. 2), the second and the third ones are parallel to the x-y plane. The anisotropic composite material properties were specified using the equations listed in the Appendix.

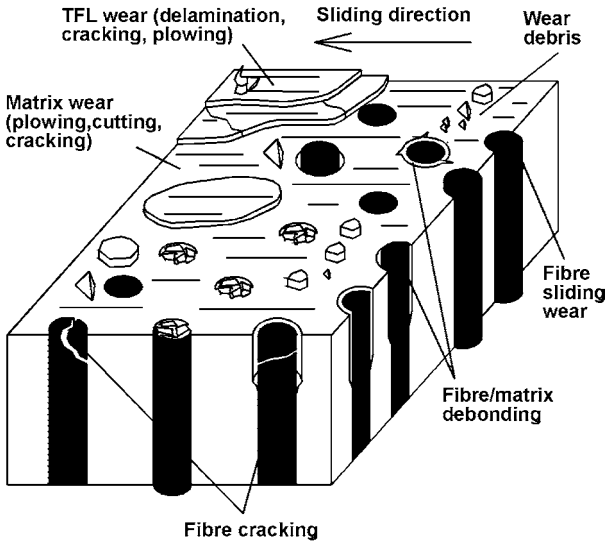

Figure 1 Typical wear mechanisms of normally oriented fibre-reinforced polymer composites (TFL = transfer film layer or compacted wear debris layer).

TABLE I Mechanical properties of the materials (σ_Y is the yield strength)

$V_f = 0.61$	Steel [6]	CF [7]	PEEK	Composite
E_{11} (MPa)	210000	235000	4030	144921
E_{22} (MPa)		15000		7276
E_{33} (MPa)		15000		7276
G_{12} (MPa)	80769	6432	1439	2734
G_{13} (MPa)		6432		2734
G_{23} (MPa)		5357		2419
ν_{12}	0.3	0.166	0.4	0.257
ν_{13}		0.166		0.257
ν_{23}		0.4		0.504
σ_Y (MPa)		—	137	—

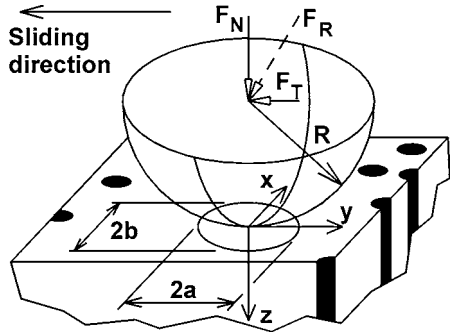

Figure 2 The modelled sliding asperity with normal and tangential loading.

The radius of the steel asperity, modelled by a hemisphere, is $R = 0.45$ mm, the normal load is $F_N = 1$ N, and the friction coefficient is $\mu = 0.45$, respectively. In the models, a larger radius was required than that of the real average asperity (some ten microns) in order to be able to compare our results with experimental test results.

To verify the simulation results and to observe the real failure mechanisms, single scratch tests were carried out. A steel ball with a diameter of 0.9 mm was compressed into the composite specimen and slid slowly. The scratched surfaces were studied by scanning electron microscopy.

The FE macro- and micro-models were created and solved by the contact and static modules of the COSMOS/M system [8].

2. FE macro and micro contact models

2.1. The displacement coupling technique

To evaluate the stresses in a fibre/matrix micro-system, firstly a FE micro-model must be created. This micro-model is "built into" a larger (homogeneous and anisotropic) macro-model to represent a larger segment of the original bodies (Fig. 3), in order to achieve a higher accuracy. Due to symmetry conditions, half of the structure is modelled, as illustrated in Fig. 3b.

In the present case, the steel asperity has a smaller elastic deformation than the composite material; therefore a small segment of the steel asperity is large enough to model the frictional contact problem. The size of the modelled asperity is 100 μm $\times$ 50 μm $\times$ 50 μm, while the size of the composite macro-model is 500 μm $\times$ 250 μm $\times$ 250 μm. The dimensions of the composite micro-model are 100 μm $\times$ 50 μm $\times$ 50 μm.

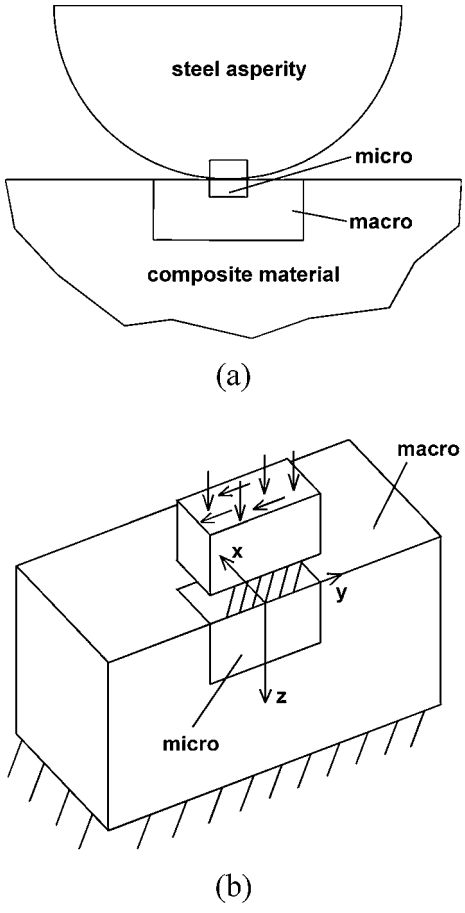

Figure 3 (a) The global model and (b) the macro/micro-models with contact elements (The arrows describe the actual loading conditions of the steel asperity).

The contact analysis operates on two levels. At first the asperity segment is "connected" to the composite macro-model by node-to-node type contact elements, while the bottom of the model is fixed, and the load is applied in the form of normal and tangential forces (Fig. 3b). The micro- and macro-models of the composite material (Fig. 3b) are fitted by the displacement coupling technique. The displacements of the points of the macro-model, located at the same planes as those of the micro-model, are assigned (by interpolation) to the micro-model as boundary conditions. These are therefore coupled surfaces. The steel asperity, on the other hand, is not split into two models because its stiffness is uniform and quite high. At both levels, the given load is applied.

2.2. The FE macro and micro contact models

Fig. 4 illustrates the FE macro contact model containing 8 node solid elements and node-to-node contact elements. The size of the contact area was pre-estimated by an analytical solution [2] in order to have a slightly greater "potential" contact area where contact elements were located. The total model contains 27454 solid elements and 156 contact elements.

If frictionless contact is studied, the contact elements are located normal to the contact surfaces. If friction is assumed they are oriented with an angle, relative

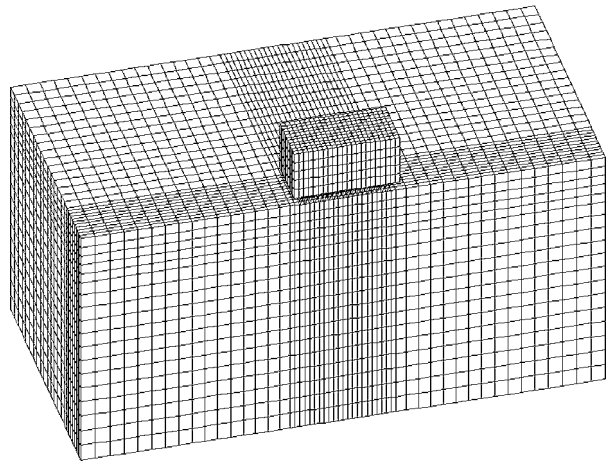

Figure 4 FE mesh of the contact macro-model (the micro-model in Fig. 5 is as large as the model of the steel segment).

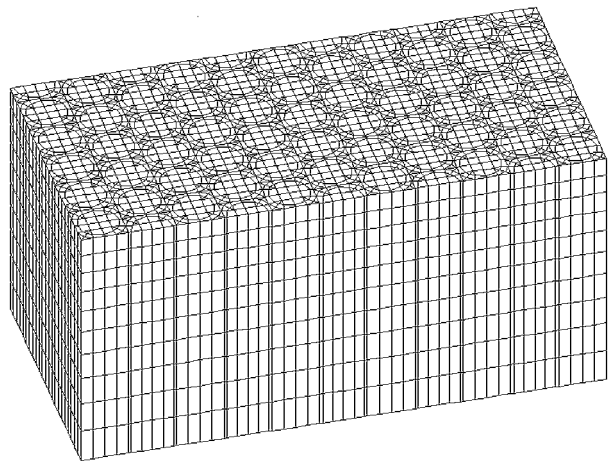

Figure 5 FE mesh of the composite micro-model (without the modelled steel asperity and the contact elements).

to the normal direction, representing the friction cone. This angle is proportional to the coefficient of friction. In other words, the direction of the contact elements is the same as the direction of the resultant force F_R, representing the normal force F_N and the friction force F_T, as shown in Fig. 2.

The anisotropic material properties of the composites and the isotropic properties of the steel are listed in Table I. The FE contact evaluation assumes a linear elastic material law.

Fig. 5 shows the composite side of the FE micro contact model. The fiber diameter is 8μm, the volume fraction is 0.61. The total model contains 40701 solid elements and 758 contact elements.

The following assumptions were used for the material models:

- Both composite components (fibre, matrix) and the steel perform in a linear elastic manner.
- The carbon fibers are transversely anisotropic, the steel counterpart and the matrix have isotropic properties.
- The fibers are in a hexagonal arrangement.
- The fibre/matrix contact is perfect.

A linear elastic material law for the matrix material was assumed because—due to the large size of the FE model (DOF > 100000)—it was not possible to provide a nonlinear FE solution assuming a linear elastic-ideal plastic material law.

3. Results

3.1. Contact results

To check the accuracy of the displacement coupling technique introduced, firstly normal contact problems (with contact elements oriented perpendicular to the contact surfaces) for different cases were solved. For each case the following contact parameters were evaluated:

- Total approach: δ,
- The major and the minor sizes of the contact area (parallel and transverse to the sliding direction) $2a$ and $2b$,
- Contact pressure distribution and its maximum: $p_{\max}$.

Contact parameters are collected in Table II. Case 1 represents the analytical solution [2] obtained for the anisotropic half-space. Case 2 shows the FE anisotropic result, for which the displacement coupling technique was used. In this case the "inner", smaller model was also an anisotropic one. Results are in good agreement, apart from the total approach that is smaller due to the smaller size of the macro-model. If only the "small" anisotropic model is considered (Case 3), the FE mesh has the same size in Fig. 4 as the size of the steel segment. As a result, the total approach is smaller, and almost the same contact parameters represent this case.

The next part of Table II refers to the micro-models. Case 4 represents the coupled model, in which the total approach and the size of the contact area are about the same as for Case 2. The contact pressure maximum is different due to the real structure where the fibers dominantly transfer the load. Case 5 contains a too small model (similar to Case 3), ignoring the effect of a larger environment. The total approach is too small, and a smaller contact area as well as higher contact pressure maximum characterize this case. Since the contact pressure maximum has a direct effect on the stress results, this difference represents the stresses too (Case 5). It can be concluded that micro-models without the coupled macro-models cannot produce reliable results.

If friction is considered (Case 6 versus Case 4), the contact parameters are different: the total approach is much higher, the contact area is wider, and the contact pressure maximum is higher. The reasons are the higher resultant force and the bending/shear type behavior of the fibers (see later).

If analytical macro-models are used and normal contact solutions are considered, such as in [2] and [4], the contact results can only poorly represent the micro system, especially in the case of friction (see e.g. contact pressure maximum values for Case 1 and Case 6).

The contact pressure distributions are shown in Fig. 6 without and with friction. In both cases mostly fibers transfer the load. The frictional force produces an asymmetric pressure distribution on each fibre loaded. The highest contact pressure appears on the rear edge of each fibre within the contact area.

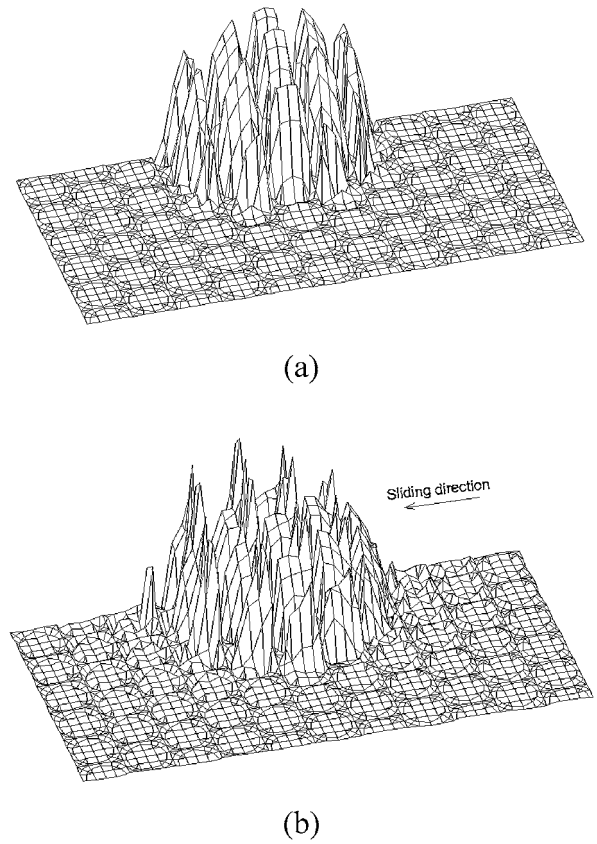

Figure 6 Contact pressure distribution (a) without friction and (b) with friction.

TABLE II Contact parameters for normal and frictional contact problems

Case number		μ	δ (μm)	$2a$ (μm)	$2b$ (μm)	$p_{\max}$ (MPa)
1	Analytical anisotropic macro-model [2]	0	0.96	41.86	41.86	1090
2	FE macro/anisotropic "small" model	0	0.88	42	43	1012
3	FE anisotropic "small" model only (with fixed boundary)	0	0.57	38	40	1335
4	FE macro/micro-model	0	0.87	40.7	41.7	1887
5	FE micro-model only (with fixed boundary)	0	0.58	36.6	36.6	2357
6	FE macro/micro-model	0.45	1.41	47.46	50.8	2562

The following displacement, strain and stress results will represent Case 6, only.

3.2. Displacement and strain results

Fig. 7 shows the deformed shape of the composite micro-structure studied. The deformed shape of the fibers is primarily caused by compression and bending/shear type loading. Considered the Figs 7–9 the deformation scale is 5 : 1.

The maximum/minimum values of strain components are collected in Table III for the fibers and the matrix respectively. Considering the fibers, the maximum shear strain γ_{yz} is produced by the frictional force. Among the maximum strain components in the matrix, γ_{yz} is the most dominant one due to its shear deformation. The second dominant strain component is ε_y in front of and just behind the contact area, with opposite signs.

Fig. 8a and b represent the γ_{yz} shear strain distribution in the matrix and the equivalent strain in the composite structure, respectively. In both cases, the maximum values appear in the contact area. In Fig. 9, a tensile strain component ε_z appears in front of the contact area. This tension "moves" the matrix material slightly up, i.e. a very small quantity of the material is "rising out" of the surface.

3.3. Stress results

The maximum/minimum stress values are collected in Table IV for the fibers and matrix respectively.

TABLE III Different strain components in the fibers and matrix

	Fibers		Matrix	
	Min	Max	Min	Max
ε_x	−0.0105	0.0062	−0.0274	0.0154
ε_y	−0.0339	0.0268	−0.0529	0.0690
ε_z	−0.0105	0.0018	−0.0270	0.0194
γ_{xy}	−0.0064	0.0324	−0.0272	0.0889
γ_{xz}	−0.0185	0.0073	−0.0473	0.0271
γ_{yz}	−0.0139	0.0764	−0.0160	0.1206
ε_{eq}	0	0.0450	0	0.0716

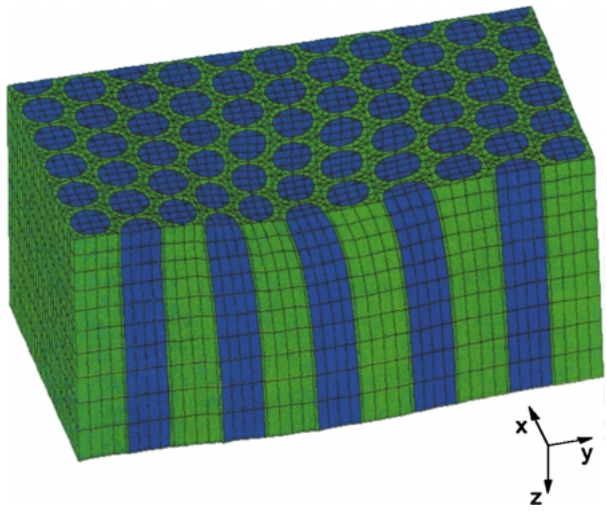

Figure 7 Deformed shape of the "micro-environment".

TABLE IV Different stress components in the fibers and matrix

	Fibers		Matrix	
	Min	Max	Min	Max
σ_x (MPa)	−224.37	100.46	−233.03	173.03
σ_y (MPa)	−598.73	394.13	−364.78	378.54
σ_z (MPa)	−2562.0	346.92	−251.42	161.34
τ_{xy} (MPa)	−34.19	173.66	−39.17	127.98
τ_{xz} (MPa)	−118.72	47.29	−68.03	38.98
τ_{yz} (MPa)	−89.57	491.38	−22.98	173.53
σ_{eq} (MPa)	0	2478	0	309.15

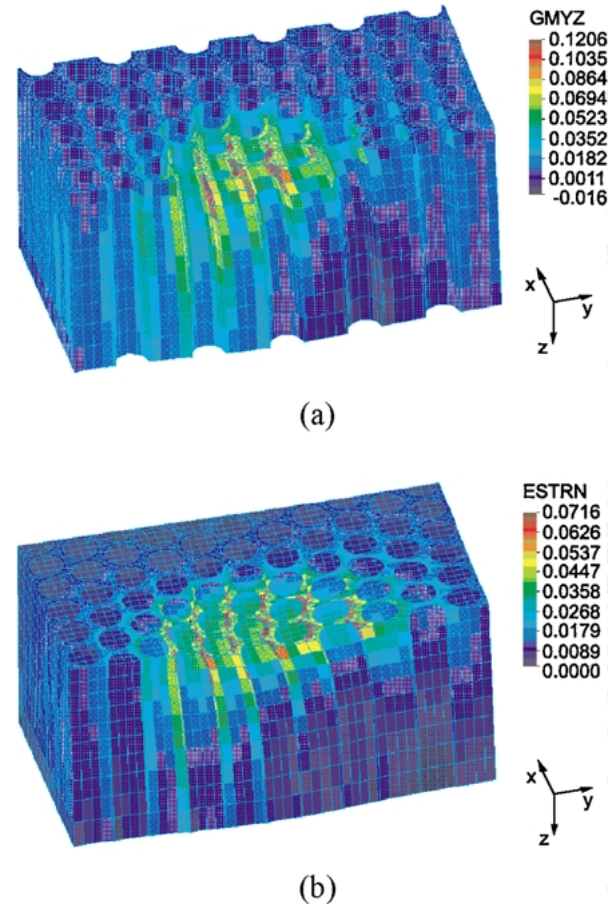

Figure 8 (a) The shear strain γ_{yz} in the matrix and (b) the equivalent strain in the composite.

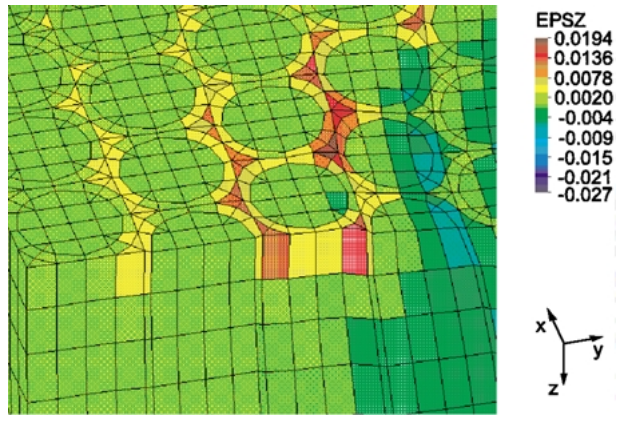

Figure 9 The strain component ε_z in the composite, in front of the contact area, sliding direction from right to left.

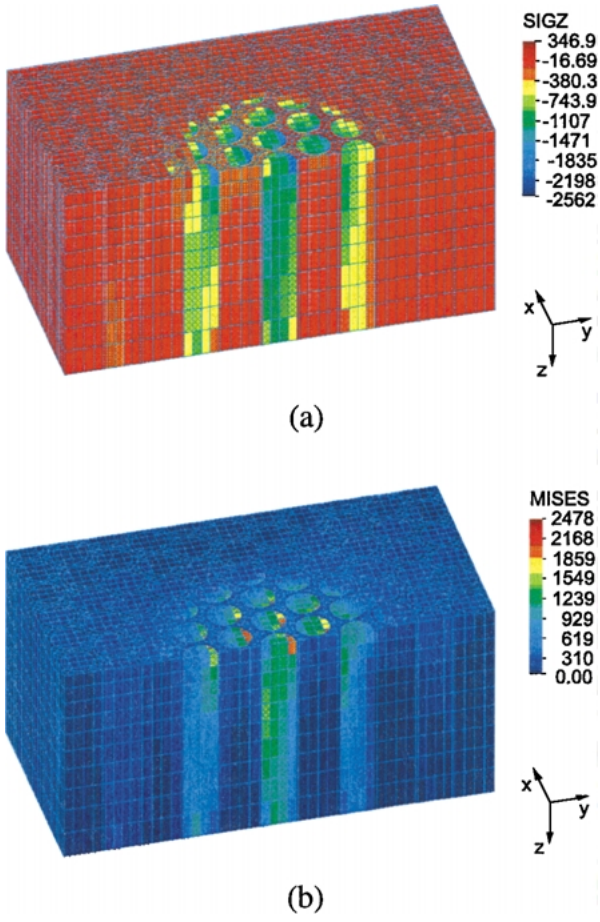

Figure 10 (a) The vertical stress component σ_z and (b) the equivalent stress distribution in the composite (in MPa).

Considering the fibers, high compressive stresses (σ_z) appear on the top of them, illustrated in Fig. 10a. In the middle of the contact area, the rear edge of each fibre is "overloaded". The same "asymmetric behaviour" is shown in Fig. 6b for the contact pressure distribution. This high stress may cause fibre cracking events at these locations. The Von Mises equivalent stresses (Fig. 10b) show similar tendencies as the compressive stresses σ_z.

According to Table IV, σ_y and τ_{yz} are the most dominant stress components in the matrix. The distribution of σ_y is presented in Fig. 11a. The highest values arise on the surface, i.e. compression in front of and tension just behind the contact area. The other dominant stress component in the matrix is τ_{yz} (Fig. 11b), having its maximum on the surface within the direct contact area. Finally, the equivalent stress in the matrix is presented in Fig. 11c. According to the equivalent stress distribution both σ_y and τ_{yz} have an effect on it. It can be established that stresses, exceeding the yield limit of the matrix material, are produced near the surface and along the fibre/matrix interfacial regions. The approximate location of the plastic zone in the matrix material can be imagined if the highest equivalent stress region is considered in Fig. 11c.

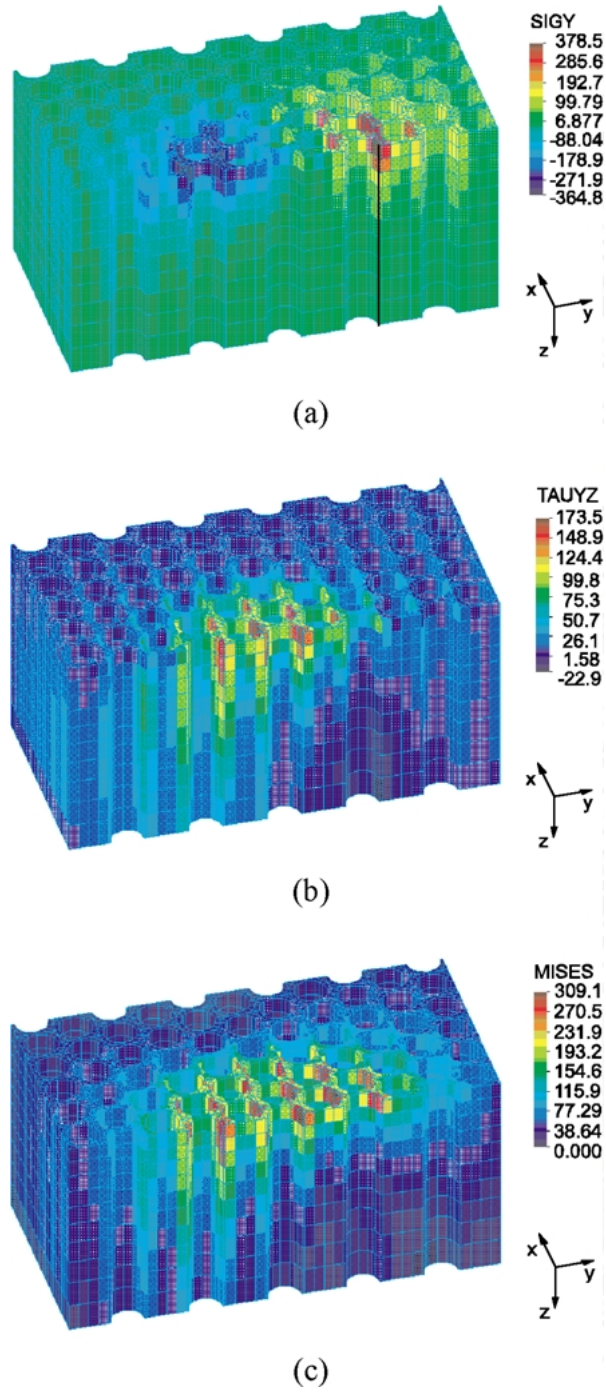

Figure 11 (a) Normal stresses σ_y, (b) shear stresses τ_{yz} and (c) equivalent stresses in the matrix (in MPa).

4. Experimental verification by scratch tests

Single scratch tests with a diamond indentor were performed on a so-called "Scratch Tribometer", which is described in Fig. 12. A small testing probe is pressed onto the surface of a specimen, using a dead weight loading arrangement. The specimen is fixed by a clamping system, which is connected to a spring element table. A connection of the latter to a load cell allows the measurement of the frictional force. On the opposite side, the probe is connected to an electrical drive by two spring elements. Vertical and horizontal movements of the probe can be realized by two slide guidances. In order to slow down the sliding speed, a gear box is fixed between the motor and the horizontal slide guidance. A defined sliding speed can be realized by a control unit. Furthermore the frictional and the normal load as well as the sliding distance can be measured and recorded by a XY-plotter.

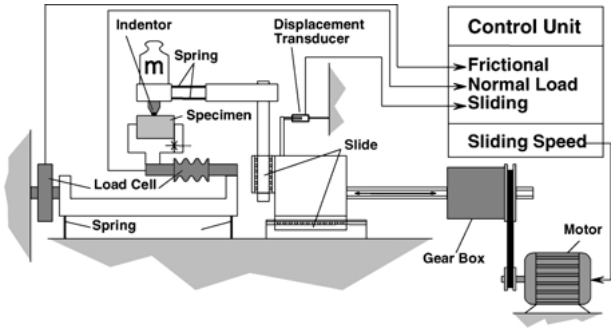

Figure 12 Scheme of the "Scratch-Tribometer".

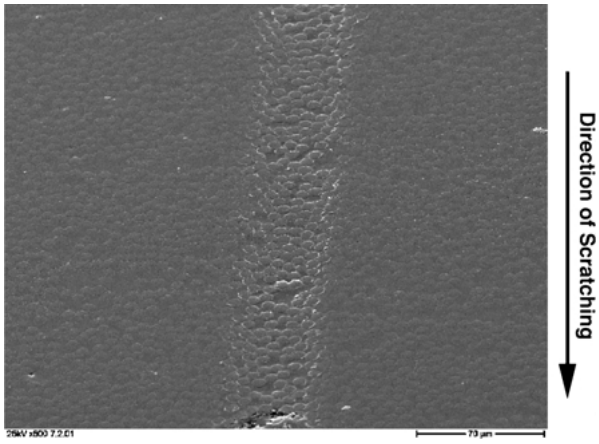

(a)

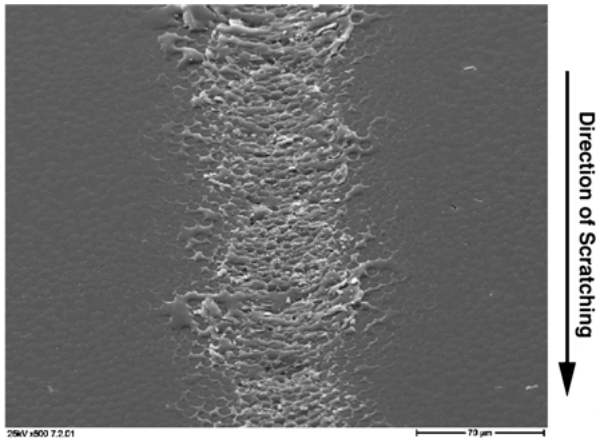

(b)

Figure 13 Low magnification SEM-micrographs of single scratch traces achieved with a diamond indentor under different loads: (a) 2 N, (b) 3 N.

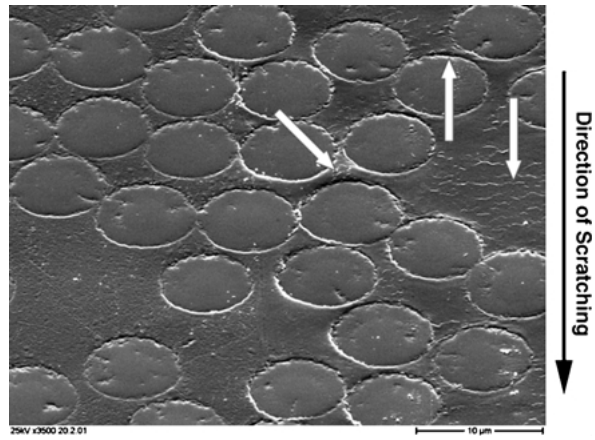

(a)

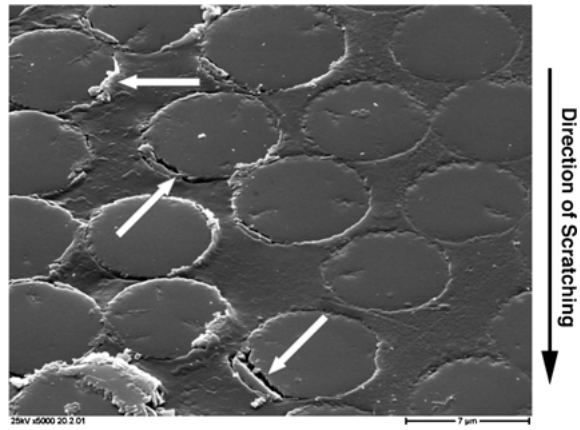

(b)

Figure 14 Higher magnification SEM-micrographs of single scratch traces achieved with a diamond indentor under different loads: (a) 1 N, (b) 2 N.

In the present testing series, normal loads, varying between 1 and 3 N, were chosen. The diamond Rockwell test indentor had a tip angle of 120° and a tip radius of 100 μm. To simulate the wear process, single scratches were produced by the indentor on the composite surfaces. Before testing, each specimen was polished with a 0.25 μm diamond paste and cleaned in an ultrasonic cleaning device.

Fig. 13 shows low magnification SEM pictures of two wear tracks achieved under two different normal loads. Fig. 14 shows higher magnification SEM-micrographs of (a) a transition between a polished, unscratched composite surface region (left side of figure, with slightly matrix below fibre level) and a diamond tip scratched region at a load of 1 N (right side, with matrix push-up, shear features and fibre/matrix debonding, see arrows), and (b) a 2 N loaded diamond tip scratch (left part of figure) with matrix push-up at fibre edges and beginning of enhanced fibre/matrix delamination and fibre edge cracking (see arrows). The right part of the figure refers to the unscratched region. And finally higher magnification SEM-micrographs of a diamond tip scratched region under 3 N load: (a) enhanced push-up of matrix between the fibers, especially visible in the transition region between the unscratched and the severely damaged center region of the groove (arrow), and (b) cracking at the rear edges of the fibers (arrows) in the center region of the diamond scratch can be seen on in Fig. 15. Using only a 1 N load leads to a rather smooth wear groove, within which only small load deformation features can be observed at higher magnification (Fig. 14a). The latter can be identified as (a) small matrix shear lips or cracks, transversely oriented to the scratch direction, (b) first indications of fibre/matrix debonding, and (c) the push-up of matrix material at the lateral fibre edges (relative to the slightly lower level of the matrix compared to the fibre ends on the polished, but unscratched composite surfaces). At the load of 2 N, these features are more and more pronounced (Figs 13a and 14b), until under 3 N first fibre cracking events appear (Figs 13b and 15). The latter occur, as expected from the FE-analysis, at the rear edges of the fibers, but also in some cases right through the fibre centers

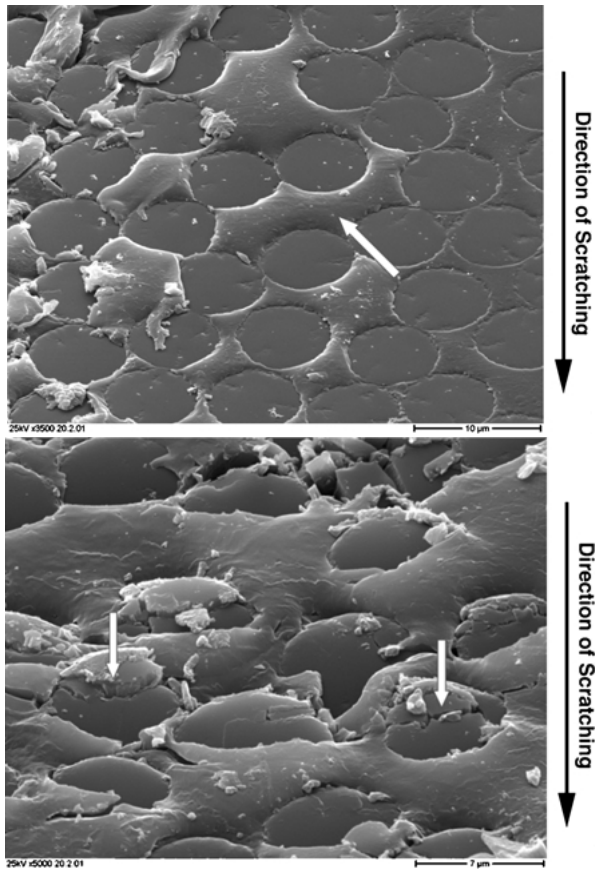

Figure 15 Higher magnification SEM-micrographs of a diamond tip scratched region under 3 N load.

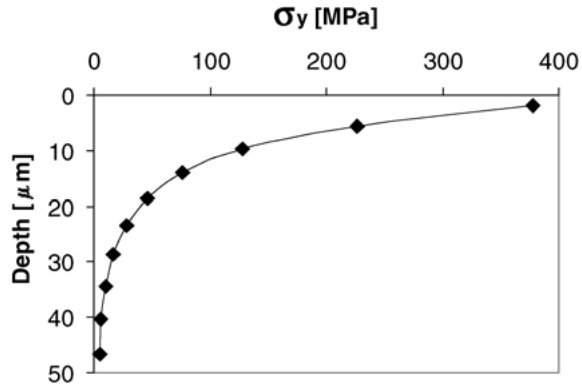

Figure 16 The horizontal stress component σ_y (producing fibre debonding) as a function of depth.

which can be expected as a result of inhomogeneities, e.g. in the form of scratches and other small defects, due to the previous polishing procedure. In addition, matrix push-up phenomena are clearly visible on both the low magnification micrograph (Fig. 13b) as well as the high magnification photos (Fig. 15). Also this is in very good agreement with the predictions made in connection with Fig. 9. Some additional experiments with a small steel ball instead of a diamond tip indentor indicated the same features, although they did not appear so clearly.

5. Discussing stress type failure conditions and wear considerations

Ovaert and Wu [4] modelled the composite material as a transversely isotropic half-space. They concluded that "the normal and tangential forces from the rough surface induce tensile stresses which reach their maximum on the composite surface and diminish with increasing depth into the composite half-space. These tensile stresses play an important role in fibre debonding".

The present micro-models can evaluate both the strain and stress components in a real fibre/matrix "micro-environment" in a more suitable way. These results can be used for further failure analysis and wear prediction.

In the case of the fibers the vertical stress component σ_z (Fig. 10a) can cause failure at the rear edges on the top of the fibers subjected to sliding contact. The compression type limit strength of CF/PEEK composite is 1200 MPa [9]. As a rough assumption the compression strength of a single carbon fibre is about 1967 MPa obtained by using a rule of mixture type relationship. This value and the maximum σ_z stress component at the rear edges of the mostly loaded fibers are about in the same range predicting fibre cracking at these local regions.

Considering the matrix material, the dominant stress components are σ_y and τ_{yz} (Fig. 11a and b) representing tension-compression and shear in the y-direction on the surface. The equivalent stress distribution (Fig. 11c) shows higher values than the yield strength of the matrix (that is 137 MPa in Table I), producing matrix yielding in the vicinity of the contact area or in the case of sliding motion in a "band" of the contact path. As a result, the matrix material becomes deformed and eventually can be sheared off in the form of thin wear debris layers (see Figs 13 to 15).

Considering the fibre/matrix structure itself, the fibre/matrix debonding should also be analyzed. In Fig. 11a, the σ_y stress components at the surface is as high as 378 MPa in the matrix near to the rear edge of the contact area. At the front edge of the contact area, in the compressed zone, the maximum value of σ_y is -365 MPa. During the sliding motion these stresses are producing a repeated compression-tension loading along the fibre/matrix interfaces at the surface, resulted debonding on both sides of these fibers (in the sliding direction). The debonding appears under lower stress level (that is less than the yield strength of the matrix material, i.e. 137 MPa) and can propagate into the subsurface. Fig. 16 shows the stress distribution along a fibre/matrix interface in the middle of the tension zone, i.e. the stress in the depth direction (cf. also Fig. 11a). The debonding depth can be approximately predicted if the debonding strength value is projected vertically until it intersects with the predicted stress-depth curve. As an example, if the debonding strength is 50 MPa, the debonding depth is about 18 μm.

One can conclude that debonding seems to be one of the first phases of the wear process. If an asperity is sliding over the same region after debonding, the stresses produced (especially in the matrix) are substantially higher due to the separate deformation of the fiber and matrix components. At the same time, stronger bonding can reduce the debonding depth and in this way, can increase the wear resistance of the composite material.

The accurate evaluation of the debonding and plastic deformation would require a CPU time consuming non-linear contact analysis. Our intention is to develop these models in the near future.

Comparing the failure mechanisms predicted, matrix shearing and fibre/matrix debonding seem to be the most dominant ones at the beginning of the wear process. These failure mechanisms were also observed in Figs 13 to 15. They are followed by fibre cracking as a further wear phenomenon because the maximum compression stress at the top of the fibers is near to the compression limit strength (see also Fig. 15).

One can conclude, therefore, that the FE macro/micro-models can detect and identify some major wear mechanisms illustrated schematically in Fig. 1.

6. Conclusions

(a) By modelling the fibre/matrix micro-structure, the FE macro/micro contact model (introducing the displacement coupling technique) introduced is much more suitable for studying failure mechanisms in the real fibre-reinforced composite than using an equivalent macro-model. As a result, the calculated contact, stress and strain results are significantly closer to real conditions.

(b) Based on the FE micro-models, possible wear mechanisms of the fibre-reinforced composite have been explored. Surface failure of the matrix material is due to high shear stresses, producing thin wear debris layers. The rear edges of the fibers located in the contact area can be cracked under high normal stresses.

(c) Regarding the failure of the fibre/matrix interface, there is a critical area where local debonding may be produced due to the high repeated compression-tension stresses. Local debonding is probably one of the starting steps of the wear process. If a partly debonded micro-structure is subjected to a repeating sliding asperity, the stresses will be even higher, thus producing more failure events in the near region of the contact area. As an additional important question, the effect of the debonding phenomena will be studied in the near future.

(d) Compared to the results of the experimental and the numerical investigations, typical failure mechanisms detected by FE models such as matrix shear failure, fibre/matrix debonding and fibre cracking were also observed on the scratched surfaces of the specimens.

Appendix

Anisotropic material properties for the composites (considering anisotropic fibre) [1]

$$E_{11} = E_{f11}V_f + E_mV_m,$$

$$\frac{1}{E_{22}} = \frac{V_f}{E_{f22}} + \frac{V_m}{E_m},$$

$$E_{33} = E_{22},$$

$$\nu_{12} = \nu_{f12}V_f + \nu_mV_m,$$

$$\nu_{13} = \nu_{12},$$

$$\nu_{23} = \nu_{f23}V_f + \nu_mV_mC,$$

$$C = \frac{1 + \nu_m - \nu_{21}\frac{E_m}{E_{11}}}{1 - \nu_m^2 + \nu_m\nu_{21}\frac{E_m}{E_{11}}},$$

$$\frac{\nu_{12}}{E_{11}} = \frac{\nu_{21}}{E_{22}},$$

$$\frac{1}{G_{12}} = \frac{V_f}{G_{f12}} + \frac{V_m}{G_m},$$

$$G_{13} = G_{12},$$

$$G_{23} = \frac{E_{33}}{2(1 + \nu_{23})},$$

where f is fibre and m is matrix.

Acknowledgements

The research presented was primarily supported by the Deutsche Forschungsgemeinschaft (DFG FR675/19-2). Furthermore, the authors would like to thank the Hungarian National Scientific Research Foundation (T 023351) and the BMBF-TéT as part of the German-Hungarian research co-operation on contact mechanics of different materials (UNG 020/99), for the additional supports.

References

1. K. K. CHAWLA, "Composite Materials" (Springer-Verlag, New York, 1987).
2. L. B. KEER and D. B. MOWRY, *Int. Jour. Solids Struct.* **15** (1979) 33.
3. T. C. OVAERT and J. P. WU, *Tribology Transactions* **36**(1) (1993) 120.
4. *Idem*; *ibid.* **37**(1) (1994) 23.
5. K. VÁRADI, Z. NÉDER, K. FRIEDRICH and J. FLÖCK *Composites Science and Technology* **59** (1999) 271.
6. VDI Wärmeatlas, 3. Auflage (1997).
7. F. N. COGSWELL, "Thermoplastic Aromatic Polymer Composites" (Butterworth-Heinemann, Oxford, 1992).
8. COSMOS/M User Guide, V2.0, Structural Research and Analysis-Corporation, 1998.
9. D. HULL, "An Introduction to Composite Materials" (Cambridge University Press, Cambridge, 1990).

Received 4 April
and accepted 9 November 2001